Microporous and Mesoporous Materials 363 (2024) 112843

Contents lists available at ScienceDirect

Microporous and Mesoporous Materials

journal homepage: www.elsevier.com/locate/micromeso

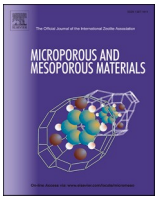

LTA zeolite particles functionalized with nanomagnetite for effective recovery of dysprosium from liquid solutions

Lorena Alcaraz [a], Belen Sotillo [b,*], Carlos Iglesias [b], Félix A. López [a], Paloma Fernández [b], Claudia Belviso [c], Ana Urbieta [b]

[a] TecnoEco Group, National Center for Metallurgical Research (CENIM), Spanish National Research Council (CSIC), Madrid, Spain
[b] Department of Materials Physics, Faculty of Physics, Complutense University of Madrid, Spain
[c] Institute of Methodologies for Environmental Analysis (IMAA), Italian National Research Council (CNR), Rome, Italy

ARTICLE INFO

Keywords:
Zeolite
LTA
Nanomagnetite
Dysprosium
Absorption

ABSTRACT

Rare earth elements (REEs) as Dysprosium (Dy) are critical elements for the fabrication of components in many green energy technologies, from electric vehicles to wind turbines. Consequently, there is an increasing interest in creating sustainable and effective materials for the recovery and recycling of these elements. Zeolite materials have demonstrated a high affinity and selectivity for REEs. Thus, this paper aims to study the use of a synthetic LTA zeolite functionalized with nanomagnetite for Dy absorption, including a complete characterization of the synthetic zeolite, the kinetics and the factors affecting the adsorption efficiency. The maximum adsorption capacity reaches a value around 35 mg of Dy per gram of zeolite. The results from the adsorption isotherms and kinetic study revealed a good agreement with both Langmuir and Temkin models and pseudo-second-order kinetics. Furthermore, the thermodynamic analysis suggests that the adsorption of Dy onto the zeolite is a spontaneous and favorable process. The findings from this work could provide insights into the design and optimization of zeolite-based processes for REE recovery and recycling, contributing to the development of a more sustainable and circular economy.

1. Introduction

The adsorption process is known as being one of the most efficient methods to recover different species from aqueous solutions such as dyes, metals and even rare earths [1–3] due to its simplicity, high efficiency, great variety of adsorbents [4]. Most studies focus their attention on the adsorption method, assessing different variables that affect the process. Among all the elements that can be recovered by an absorption process, this study will be focused on rare earth elements (REEs), which are crucial components for many modern technologies, and specifically on the recovery of Dysprosium (Dy). Dy can be found as a component of laser materials, in alloys of nuclear reactors, or in magnets used for cars, electronic vehicles or wind turbines [5]. However, the extraction and separation of Dy from natural resources can be challenging and costly due to its low concentration [5]. Additionally, the mining and processing of REEs can lead to environmental damage and public health risks. In this scenario, zeolites, thanks to their porosity and physico-chemical properties can be outstanding candidates to recover this precious REE [6].

Zeolites are characterized by a three-dimensional structure made up of tetrahedral networks of ions $[SiO_4]^{4-}$ and $[AlO_4]^{5-}$ linked by oxygen atoms (Fig. 1). Due to this structure, zeolites have microcavities partially or totally connected by channels; which allows them to have a large internal effective surface [7,8]. Beside natural zeolites, there are many synthetic equivalents exhibiting similar or even better properties than natural ones [8]. Due to their tunable characteristics, both materials are used in diverse applications: catalysis, gas sensing, cleaning of polluted water, soil remediation, rare earth adsorption or medical treatments [7,8].

In this work, the properties of a Zeolite Linde Type A (LTA Zeolite or Zeolite A) [9] functionalized with nanomagnetite have been studied and its efficiency in dysprosium adsorption from a solution is analyzed. The empirical formula of this type of zeolite is $[Me_x][Al_{12}Si_{12}O_{48}]$, being Me a metal cation [10] (in our case, sodium). This synthetic zeolite is formed by two cage types: β-cage (sodalite cage), and α-cage, this last constructed by the connection of eight sodalite cages (Fig. 1). The

* Corresponding author.
E-mail address: bsotillo@ucm.es (B. Sotillo).

https://doi.org/10.1016/j.micromeso.2023.112843
Received 27 July 2023; Received in revised form 4 October 2023; Accepted 6 October 2023
Available online 7 October 2023

functionalization of the zeolite with nanomagnetite [11] will allow the easy recovery of the sample from the solution after the adsorption process. This points toward a green circular economy model that, according to the EU [12], is a model based on production and consumption designed to extend the cycle life of existing products. Also, this zeolite is characterized by good thermal and mechanical stability [10,13], making it a good candidate to perform adsorption experiments.

2. Materials and methods

2.1. Synthesis and characterization

Zeolite sample used in this work was synthesized by hydrothermal method at 60 °C as described in Belviso et al., 2020 [11], using pure reagents (sodium silicate and sodium aluminate) with the addition of synthetic nanomagnetite. All chemicals of reagent grade were purchased from Aldrich Chemicals Ltd.

The mineralogical composition of the synthetic product was analyzed by X-ray powder diffraction (XRD) using a Rigaku Rint 2200 powder diffractometer with Cu-Kα radiation. The XRD patterns were collected in the angular range 2θ 3–70°, step-size of 0.02, scan-step time of 3 s, accelerating voltage of 40 kV and electric current of 30 mA. The morphology of the sample was studied by Scanning Electron Microscopy (SEM) in a SEM FEI Inspect microscope working at 15 kV. Fourier-transformed infrared spectroscopy (FTIR) measurements were performed using a Varian 670 FTIR spectrometer within the frequency range 4000–400 cm^{-1} in transmittance mode with a spectral resolution of 4 cm^{-1}. Measurements were carried out using the KBr pellet technique. Characterization by Raman spectroscopy (RS) and cathodoluminescence (CL) were also performed. A Horiba JobinYvon confocal microscope LABRAM-HR equipped with a He–Ne laser (633 nm) and a He–Cd laser (325 nm) was used for RS measurements. Depending on the excitation laser, either an Olympus visible 10 × objective (0.25 NA) or an UV objective 40 × ThorLabs (0.47 NA) was used. The Raman signal was measured with an air-cooled CCD camera. For CL, a SEM microscope Hitachi S2500 with an acceleration voltage of 15 kV was employed, and the luminescence signal was recorded with a CCD HAMAMATSU PMA-12 (measuring range from 200 nm to 900 nm) coupled to an optical fiber. The magnetic properties were measured at room temperature (298 K) in an A JDAW-2000D-type Vibrating Sample Magnetometer (VSM). Finally, Dysprosium concentrations in the solutions were analyzed by Inductively Coupled Plasma-Optical Emission Spectrometry (ICP-OES) using an Agilent ICP-OES (Agilent Technologies, Sana Clara, CA, USA), model 5100 VDV (Vertical Dual View).

2.2. Adsorption experiments

The dysprosium adsorption experiments were carried out via *batch* experiments. Initially, 1 g L^{-1} stock solution was prepared by dissolving ($Dy(NO_3)_3{\cdot}xH_2O$) in MilliQ water. Subsequently, the stock solution was diluted to obtain dysprosium solutions with 5 mg L^{-1} (ppm) concentration. Initially, 30 mg of zeolite were put in contact with 100 mL of the dysprosium solutions until equilibrium was reached. The temperature was controlled using a Selecta Termotronic thermostat bath equipped with multiple Lab Companion MS-52 M stirrers for the tests. Aliquots of the solution were extracted and filtered through a syringe filter with a 0.22 μm pore, and 13 mm diameter. Then, dysprosium concentration in the filtered solution was measured. The dysprosium adsorbed percentage was calculated using *Equation (1):*

$$\text{Adsorbed Dy}\ (\%) = \frac{(c_0 - c_t)}{c_0} \cdot 100 \qquad \text{(Eq. 1)}$$

where c_0 ($mg{\cdot}L^{-1}$) is the initial concentration of dysprosium, and c_t ($mg{\cdot}L^{-1}$) is the concentration of dysprosium in solution at time *t*.

The adsorption capacity of zeolite at each time t (q_t ($mg{\cdot}g^{-1}$)) was obtained by *Equation (2)*:

$$q_t = \frac{(c_0 - c_t) \cdot V}{m} \qquad \text{(Eq. 2)}$$

where V (L) is the volume of the solution, and m (g) is the mass of the zeolite added in the tests.

Linear and nonlinear kinetics studies were carried out at different temperatures, fitting the experimental data to the pseudo-first and pseudo-second order models [14–17], according to *Equations 3 to 6* (see Table 1).

Where q_e ($mg{\cdot}g^{-1}$) is the amount of dysprosium adsorbed by mass of the zeolite at the equilibrium; and k_1 (min^{-1}) and k_2 ($g{\cdot}mg^{-1}{\cdot}min^{-1}$) are the first and the second order adsorption constants, respectively.

Equilibrium adsorption isotherms have been studied using linear and

Table 1
Equations employed to perform the kinetic studies of the adsorption process.

	Equation	
Pseudo first order		
linear	$\ln(q_e - q_t) = \ln q_e - k_1 \cdot t$	*(Eq. 3)*
nonlinear	$q_t = q_e(1 - e^{-k_1 \cdot t})$	*(Eq. 4)*
Pseudo second order		
linear	$\frac{t}{q_t} = \frac{1}{k_2 \cdot q_e^2} + \frac{1}{q_e} t$	*(Eq. 5)*
Nonlinear	$q_t = \frac{k_2 \cdot q_e^2 \cdot t}{1 + k_2 \cdot q_e \cdot t}$	*(Eq. 6)*

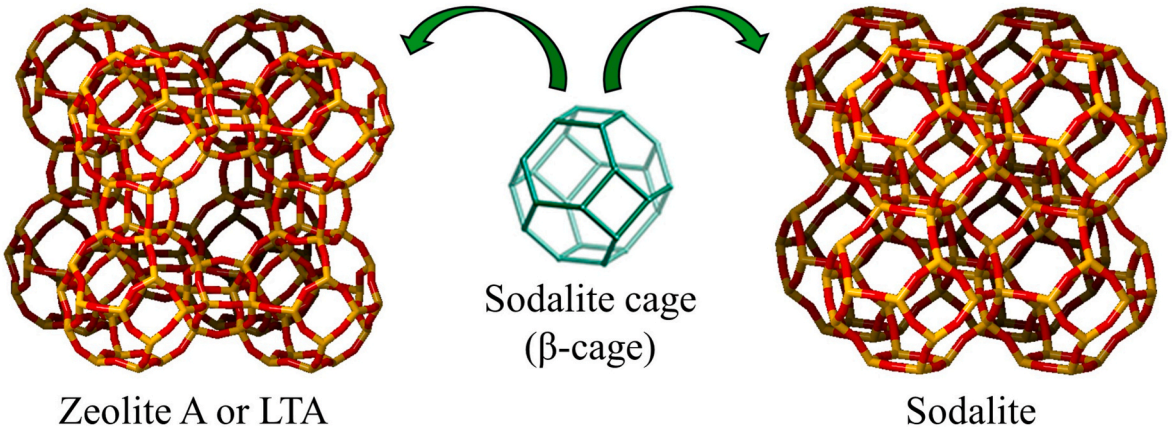

Fig. 1. Frameworks of two types of zeolites, which are formed from the basic structure of a sodalite cage. The images obtained from 3D drawing tool in the International Zeolite Association IZA [9].

non-linear forms of Langmuir, Freundlich, Temkin and Dubinin-Radushkevitch (DR) models, *Equations 7-14* (see Table 2) [18–21]. To perform this analysis, 10 mg, 20 mg, 30 mg, and 40 mg of zeolite were put in contact with 100 mL solution containing 5 mg L^{-1} of dysprosium ions, at room temperature (298 K) until equilibrium was reached.

In these equations, adsorption capacities q are expressed in mol·kg^{-1} and concentrations c in mol·L^{-1}, by using the molecular weight of Dy, 162.5 g/mol. In the Langmuir model, q_m is the maximum adsorption capacity of the adsorbent per unit mass of adsorbate and K_L (L·mol^{-1}) is the Langmuir constant. In the Freundlich model, K_F (L·kg^{-1}) is the Freundlich constant and n (dimensionless) is the Freundlich constant related to the adsorption intensity.

In the Temkin model, A_T (L·kg^{-1}) is the Temkin isotherm equilibrium binding constant; and q_T, which has the same units as q_e, is given by *Equation (15)*:

$$q_T = q_m \cdot \frac{R \cdot T}{B_T} \quad \text{(Eq. 15)}$$

where R = 8.314 × 10^{-3} kJ K^{-1} mol^{-1} is the universal gas constant, T (K) is the absolute temperature, and B_T (kJ·mol^{-1}) is the Temkin isotherm constant.

Finally, q_{DR} (mol·kg^{-1}) is the theoretical adsorption isotherm saturation capacity, β (mol^2/kJ^2) is the DR isotherm constant and ε is the Polanyi potential, given by *Equation (16)*:

$$\varepsilon = RT \ln(1 + 1/c_e) \quad \text{(Eq. 16)}$$

The standard Gibbs free energy change (ΔG^0, kJ·mol^{-1}) of the process is calculated using the equilibrium constant obtained from the best-fitted isotherm model and applying the Van't Hoff equation model (*Equation (17)*) [22,23]:

$$\Delta G^0 = -RTln\left(K_e^0\right) \quad \text{(Eq. 17)}$$

where K_e^0 is the thermodynamic equilibrium constant.

Finally, Weber–Morris intraparticle diffusion model was used to evaluate the intraparticle diffusion resistance that influences the adsorption process, according to Equation (18) [24]:

$$q_t = k \cdot \sqrt{t} + C \quad \text{(Eq. 18)}$$

where q_t is the adsorbed quantity, k (mg·g^{-1}·$min^{-0.5}$) is the intraparticle diffusion rate constant, and C (mg/g) represents the boundary effect (resistance to the mass transfer that is related to the thickness of the boundary layer.

Table 2
Equations employed to perform the adsorption isotherm analysis [16].

Adsorption isotherm		
Langmuir model		
Linear	$\frac{c_e}{q_e} = \frac{1}{q_m \cdot K_L} + \frac{1}{q_m} \cdot c_e$	*(Eq. 7)*
Nonlinear	$q_e = \frac{q_m K_L c_e}{1 + K_L c_e}$	*(Eq. 8)*
Freundlich model		
Linear	$\ln q_e = \ln K_F + \frac{1}{n} \cdot \ln c_e$	*(Eq. 9)*
nonlinear	$q_e = K_F \cdot c_e^{1/n}$	*(Eq. 10)*
Temkin model		
linear	$q_e = q_T \cdot \ln A_T + q_T \cdot \ln c_e$	*(Eq. 11)*
nonlinear	$q_e = q_T \cdot \ln (A_T \cdot c_e)$	*(Eq. 12)*
Dubinin-Radushkevitch model		
linear	$\ln q_e = \ln q_{DR} - \beta\varepsilon^2$	*(Eq. 13)*
Nonlinear	$q_e = q_{DR} \cdot \exp(-\beta\varepsilon^2)$	*(Eq. 14)*

3. Results and discussion

3.1. Synthetic zeolite characterization

Fig. 2a shows XRD pattern of synthetic LTA. Peaks marked with a diamond (◆) may be ascribed to the LTA zeolite, while those marked with a cross (×) are associated to the nanomagnetite particles used to functionalize the zeolite sample. EDX spectra (Fig. 2b) indicates that the Si/Al ration of the synthetic zeolite is close to 1, and also confirms the incorporation of Fe into the samples or precipitated on the surfaces. SEM images (Fig. 3) indicate a spherical/cubic shape of newly formed mineral with diameters ranging from 0.5 to 2 μm.

Raman spectrum for 325-nm excitation and 633-nm excitation are shown in Fig. 4a and b, respectively. UV-Raman spectrum is composed of three equidistant peaks at 493, 1079, and 1592 cm^{-1}. The peak at 493 cm^{-1} is attributed to the bending of the SiO–Al rings with an even number of components that appear in the structure of zeolites [25,26]. Since the peaks at 1079 and 1592 cm^{-1} appear equally spaced, doubling or tripling the frequency of the mode at 493 cm^{-1}, it was assumed that they are resonant replicas of this mode [27]. Besides, bands around 1000 cm^{-1} (980, 1068 y 1079 cm^{-1}) are ascribed to asymmetric stretching modes of T-O structures, being T atoms of Si or Al [25,26]. On the other hand, in the red-Raman spectrum, two main peaks can be identified, at 493 cm^{-1} and at 665 cm^{-1}. The first one is again associated with the vibrations of the zeolite structure, whereas the 665 cm^{-1} is related to nanomagnetite particles [28,29] thus confirming the effective inclusion of the nanomagnetite into the zeolite A or precipitated on the surface. Fig. 4c exhibits the FTIR spectra of the synthetized zeolite. The principal information of the structure is in the range 1400-400 cm^{-1} [30,31]. The band centered at 467 cm^{-1} is related to vibrations internal to Si–O and Al–O tetrahedra. The more intense band at 560 cm^{-1} is related to the presence of the double rings (D4R and D6R) in the framework structures. In addition, the absorption band centered at around of 666 cm^{-1} can be assigned to the symmetrical stretching vibrations of the ν_s Si–O–Al bond bridges. The large broad band at 1004 cm^{-1} can be attributed to the overlap of the asymmetric stretching vibrations characteristic of ν_{as} Si–O (Si) and ν_{as} Si–O (Al) bridge bonds in TO_4 tetrahedra belonging to aluminosilicates with zeolite or sodalite structure. The band at 1450 cm^{-1} can be assigned as –OH bending due to the scissoring mode of vibration. Finally, the observed bands around 1650 cm^{-1} and 3430 cm^{-1} are attributed to the bending of the OH group, and the asymmetric stretching mode of molecular water coordinated to the edges of the zeolite channels in adsorbed water, respectively. This interaction can be attributed to the adsorption of water molecules in the zeolite cavities by physisorption [32]. The obtained results are in good agreement with the XRD and Raman results data.

CL spectrum recorded on the zeolite samples is presented in Fig. 5. The emission consists of a broad band between 200 nm and 600 nm. To our knowledge, literature data devoted to luminescence of zeolite A itself have not been published. Some information about the luminescence can be extracted by studying the luminescence of the constituents: aluminates and silicates. Then, three contributions can be identified in this broad band. First, at 345 nm, it may be related to O vacancies in aluminates [33]; the second, at 360 nm, appears associated to recombination of electron-hole pairs in silicates [34]; the third, at 403 nm, may be linked to defects associated with OH groups in silicates [35]. These measurements, in combination with the observed resonant Raman for excitation with 325 nm wavelength, indicate that the obtained zeolites have a wide bandgap, as expected for zeolite materials [36]. Therefore, XRD, Raman and luminescence measurements confirm the crystal structure of zeolite A and its functionalization with nanomagnetite. They also assess the good quality of the obtained zeolites.

The magnetic properties of the obtained zeolite were analyzed using the VSM curves as shown in Fig. 5b. In the present case, the magnetization of the sample increases with the magnetic field. The saturation magnetization (Ms) is 1.95 emu/g. The low value of magnetization

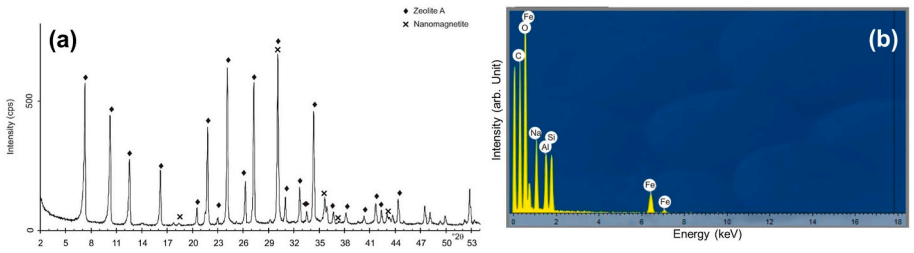

Fig. 2. (a) XRD pattern and (b) EDX spectra of the synthetic zeolite.

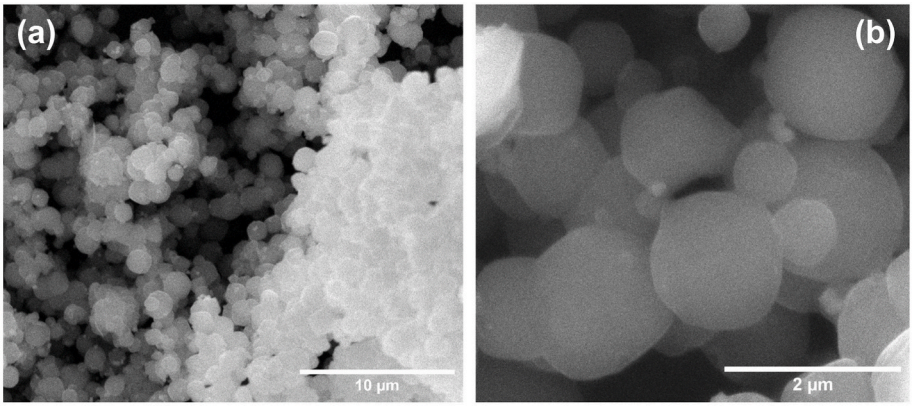

Fig. 3. SEM images of the zeolites samples: (a) low magnification; (b) high magnification.

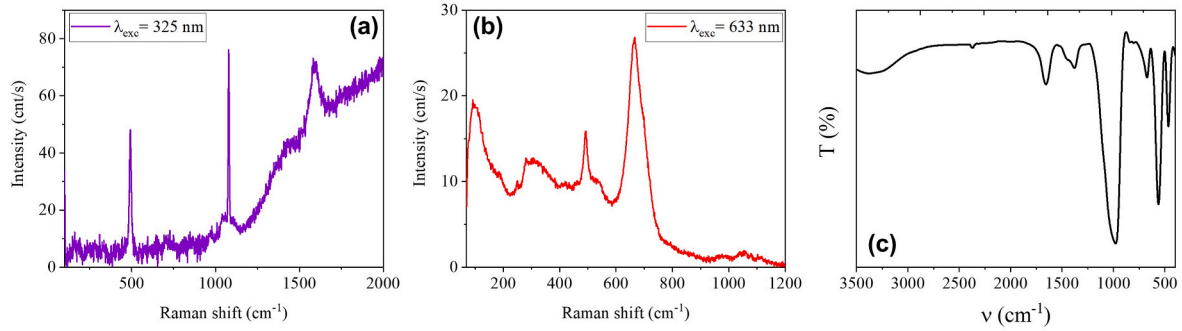

Fig. 4. Raman spectra of the obtained zeolite samples: (a) with excitation wavelength of 325 nm; (b) with excitation wavelength of 633 nm. (c) FTIR of the sample.

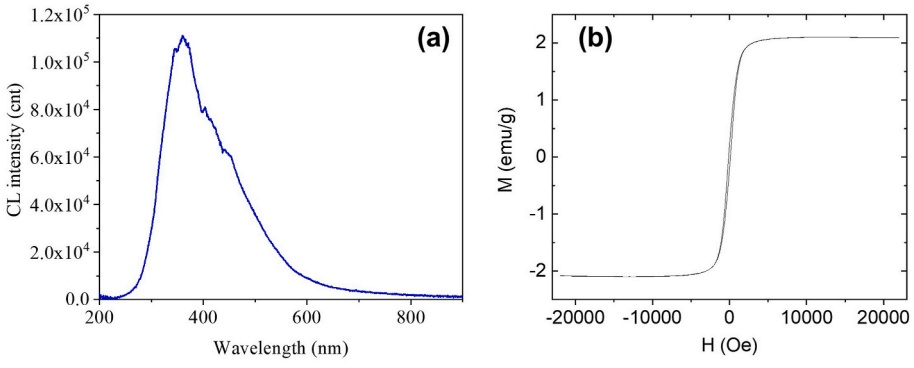

Fig. 5. (a) CL spectrum recorded on zeolite sample at room temperature with an acceleration voltage of 15 kV. (b) VSM curve recorded for the synthetic zeolite.

observed is probably due to the small amount of magnetite functionalizing the zeolite, in good agreement with the XRD measurements (see Fig. 2a). Despite this value, the coercivity field (Hc) was 115 Oe, and remanent magnetization (Mr) 1.7 emu/g, showing the typical superparamagnetic behavior of magnetite.

3.2. Adsorption experiments

The behavior of dysprosium in solution is a complex phenomenon because it could be present as cation, or as hydroxide cation depending on the pH value [37]. The predominant specie is Dy^{3+} at acid pH values, which hydrolyzed leading to the formation of other hydroxides species when the pH increases. For the initial tests, 30 mg the zeolite A were put in contact with 5 mg L^{-1} concentration dysprosium solution for 180 min after the pH value was adjusted to 1.5, using a HNO_3 (0.1 M) solution. After that, dysprosium concentration in the solution was measured. We have observed that in these acid conditions, the adsorption capacity of the zeolites was low, with adsorption percentages lower than 5%. We associate this phenomenon with a degradation of the zeolite samples, as it was not possible to recover the material after these experiments.

In order to increase the dysprosium adsorption, 30 mg of zeolite were put in contact with 5 mg L^{-1} concentration of dysprosium solutions. For that, the tests were carried out without varying the pH value. Thus, the pH value was measured resulting in an approximate value of 6, similar to the pH value reported for other REE elements [38,39]. After a contact time of 180 min, dysprosium adsorption percentages were calculated. At pH 6 the adsorption percentage clearly increases, reaching a value of almost 100% in the experimental conditions used (99.4%). Then, the equilibrium conditions were fixed to 30 mg of zeolite, 5 mg L^{-1} of dysprosium solution, pH of 6 and 180 min of contact time.

3.3. Effect of the temperature and kinetic study

To evaluate the influence of temperature on the adsorption process, experiments at different temperatures (298, 313, and 328 K) were carried out. 30 mg of the zeolite were put in contact with a 5 mg L^{-1} dysprosium solution for the tests. The results obtained are shown in Fig. 6. Similar behavior was found at the different temperatures investigated. The equilibrium was reached at around 90 min. Within the temperature range considered, similar adsorption capacities were found with the increase of the temperature, thus, the temperature does not seem to play a significant role in our experiments. Thus, the average dysprosium adsorption capacity by the zeolite was at around 16 mg g^{-1}.

Adsorption kinetics studies were analyzed by using *Equations 3-6* (Fig. 7). The best fitted results (Table 3) were found for a pseudo-second-order model for all temperatures studied. The pseudo-second-order kinetic reaction constants (i.e. k_2) slightly increase with the temperature. This result shows that the increase in the temperature does not practically affect the dysprosium adsorption process by the zeolite.

As observed by other authors [40], the fit of the data to the pseudo-first order model show a significant improvement respect to the linearized model. Nevertheless, in the non-linear fit, pseudo-second order model still has more probability to be correct that the pseudo-first order model. To compare both model, we have employed two statistic parameters: the adjusted determination coefficient (R^2_{adj}) and the Akaike's information criterion (AIC) [41]. For the three temperature studied, $(R^2_{adj})_{second} > (R^2_{adj})_{first}$ and $AIC_{second} < AIC_{first}$, which is a clear indication of the better accuracy of the pseudo-second order model.

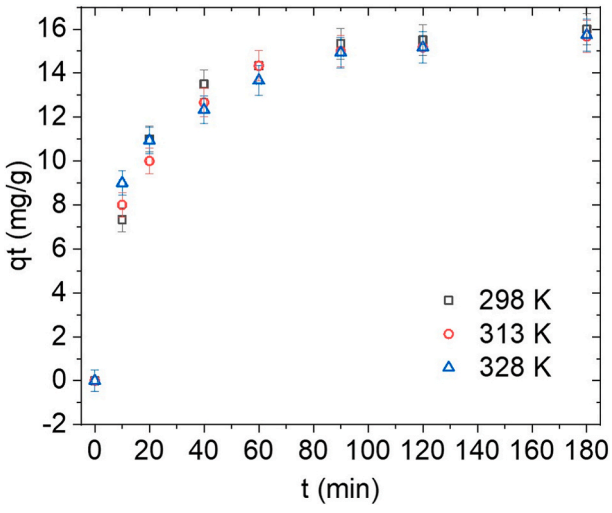

Fig. 6. Dysprosium adsorption capacities of the recovered zeolite at different temperatures.

3.4. Equilibrium isotherms and thermodynamic study

Equilibrium isotherms at 298 K (Fig. 8) were analyzed by varying the amount of the zeolite, according to *Equations 5* to *7*. The calculated parameters for the different models studied, and the corresponding correlation coefficients are summarized in Table 4.

The best fit was found for the Temkin model, but closely followed by Langmuir model. Langmuir model assumes independent adsorption sites and a monolayer coverage, whereas Temkin model was developed assuming that the adsorption heat decreases linearly with the increase of the adsorbent coverage of the surface [20,42,43]. Temkin model shows the higher value of R and the smallest AIC value, indicating that this model is more likely to be correct. It is also interesting to point out that, for Temkin model, both linear and non-linear fit produce almost equal values for the quantities in the equation. Different constants can be calculated from the Temkin isotherm fit according to *Equations 10* and *15*. The calculated values for Temkin isotherm equilibrium binding constant A_T and q_T were 3.9×10^6 L mol^{-1}, and 0.048 mol kg^{-1}. If we consider the value obtained from the Langmuir model $q_m = 0.217$ mol kg^{-1}, we can estimate the value of B_T, which is related to the heat of sorption (*Eq. (15)*) [44]. In the present case, the obtained value for the heat of sorption constant is 11.2 kJ mol^{-1} (or 2.68 kcal mol^{-1}). Thus, physical adsorption occurs (physisorption process) when the calculated heat of sorption value is lower than 4.18 kJ mol^{-1} (1.0 kcal mol^{-1}). On the other hand, the chemical adsorption (chemisorption process) occurs when the calculated value is between the range of 83.68–209.20 kJ mol^{-1} (20–50 kcal mol^{-1}). Finally, both, physisorption and chemisorption processes are involved when the calculated obtained value is between 4.18 and 83.68 kJ mol^{-1} (1–20 kcal mol^{-1}) [44]. As stated above, in the present case, the value calculated for the heat of sorption constant is 11.2 kJ mol^{-1}, indicating that both processes are involved in the dysprosium adsorption by the zeolite.

On the other hand, Langmuir equilibrium constant K_L can be used to estimate de Gibb's free energy change using Van't Hoof equation (*Eq. (17)*). According to Liu [22], for dilute solutions of charged adsorbates (in our case Dy^{3+} with concentration of 3.1×10^{-5} mol/L), K_e^0 can be reasonably approximated by the Langmuir equilibrium constant if it is expressed in L/mol ($K_L = 4.2 \times 10^5 \frac{L}{mol}$) and transformed into a dimensionless value by multiplying by the standard concentration of the adsorbate ($[adsorbate]^0$, by definition is 1 mol/L) and considering the activity coefficient γ of the adsorbate equal to 1 [23]:

$$K_e^0 = \frac{1000 \bullet K_L \bullet adsorbate\ molecular\ weigth \bullet [adsorbate]^0}{\gamma}$$

Then,

$$\Delta G^0 = -RTln\left(K_e^0\right) = -32.1\ kJ\ /\ mol$$

The value obtained for the Gibb's free energy change is negative, which indicates that the Dy adsorption process is spontaneous and favorable.

Finally, the adsorption capacities of different adsorbents for Dy^{3+} are compared in Table 5. It should be noted that the adsorption process strongly depends on the experimental conditions, making the comparison of the adsorption process complex. Table 5 reveals that the obtained

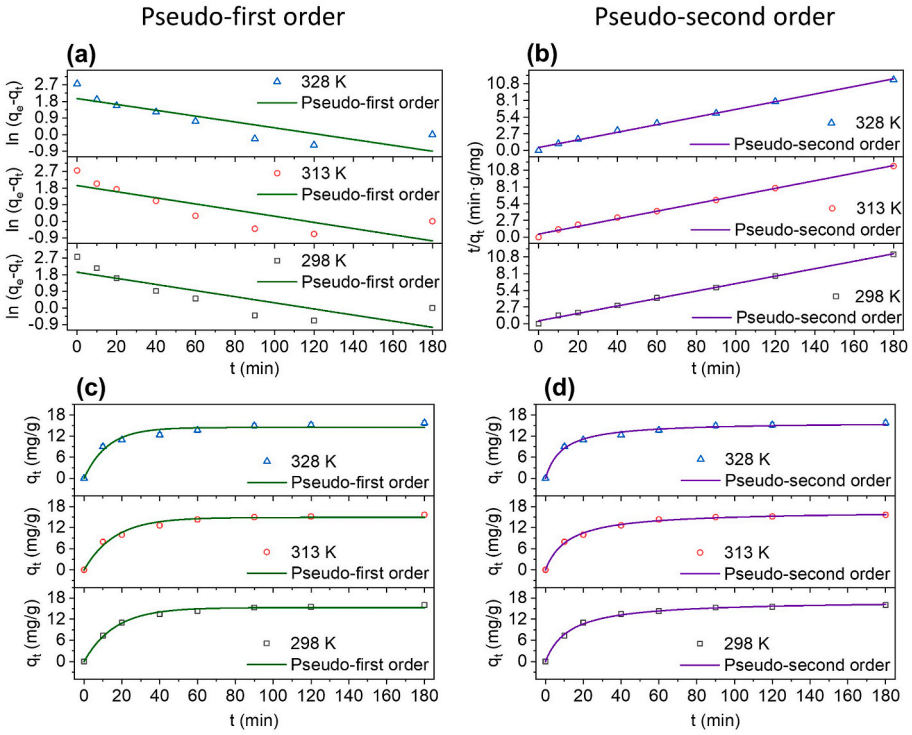

Fig. 7. Pseudo-first (a), and pseudo-second (b) order adsorption kinetics models at different temperatures.

Table 3
Calculated kinetics parameters at different temperatures.

Linear fitting						
T (K)	Pseudo-first-order			Pseudo-second-order		
	k_1 ($\times 10^{-3}$ min^{-1})	q_e (mg/g)	R^2_{adj}	k_2 ($\times 10^{-3}$ g/mg·min)	q_e (mg/g)	R^2_{adj}
298	16.2	6.96	0.63	7.50	16.61	0.996
313	17.6	6.91	0.63	7.52	16.21	0.996
328	17.9	7.07	0.68	7.92	16.18	0.996
Non-linear fitting						
T (K)	**Pseudo-first-order**			**Pseudo-second-order**		
	k_1 ($\times 10^{-3}$ min^{-1})	**q_e (mg/g)**	**R^2_{adj}**	**k_2 ($\times 10^{-3}$ g/mg·min)**	**q_e (mg/g)**	**R^2_{adj}**
298	62.2	15.31	0.996	4.63	17.33	0.998
313	62.6	14.90	0.98	4.99	16.76	0.997
328	80.9	14.45	0.96	7.08	16.04	0.994

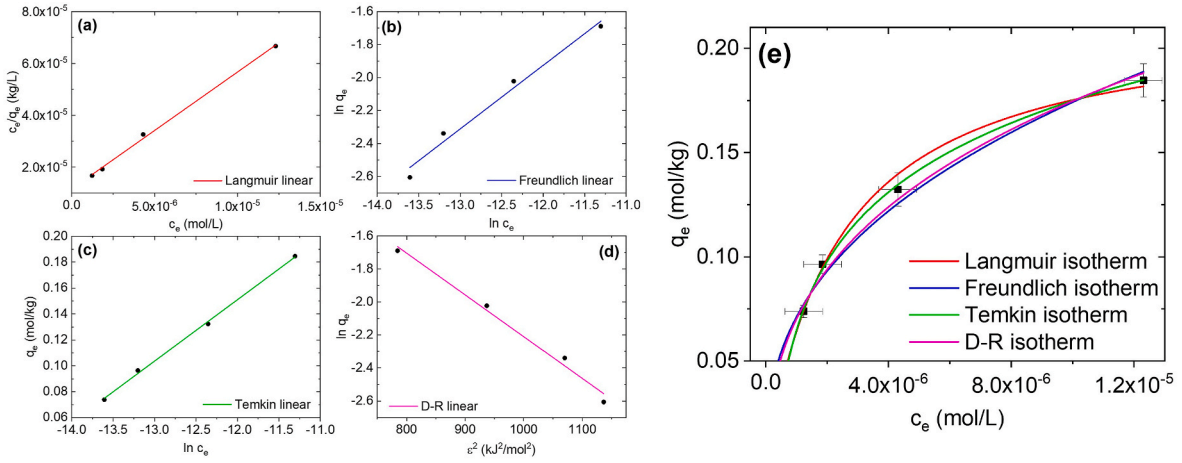

Fig. 8. Linear Langmuir (a), Freundlich (b), Temkin (c) and Dubinin-Radushkevitch (d) adsorption isotherms at 298 K. (e) Non-linear isotherm for the four models.

Table 4
Calculated parameters for the Langmuir, Freundlich, Temkin and Dubinin-Radushkevitch models, from both linearized and non-linearized equations.

Linear fitting							
Langmuir		Freundlich		Temkin		Dubinin-Radushkevitch	
q_m (mol/kg)	0.222	n	2.59	q_T (mol/kg)	0.047	q_{DR} (mol/kg)	1.38
K_L (L/mol)	3.9×10^5	K_F (L/kg)	14.84	A_T (L/mol)	3.9×10^6	β (mol^2/kJ^2)	0.0025
R^2_{adj}	0.997	R^2_{adj}	0.97	R^2_{adj}	0.998	R^2_{adj}	0.98
Non-linear fitting							
Langmuir		**Freundlich**		**Temkin**		**Dubinin-Radushkevitch**	
q_m (mol/kg)	0.217	n	2.57	q_T (mol/kg)	0.048	q_{DR} (mol/kg)	1.39
K_L (L/mol)	4.2×10^5	K_F (L/kg)	15.3	A_T (L/mol)	3.9×10^6	β (mol^2/kJ^2)	0.0026
R^2_{adj}	0.997	R^2_{adj}	0.98	R^2_{adj}	0.999	R^2_{adj}	0.992
AIC	22.51	AIC	29.04	AIC	17.83	AIC	27.47

Table 5
Comparison of adsorption capacity with other adsorbents.

pH	T (K)	Contact time (min)	Adsorption capacity (mg/g)	Adsorbents	References
4	333	120	33.52	Physically activated carbons	[2]
4	333	120	31.26	Chemically activated carbons	[2]
–	273	120	23.20	Functionalized and modified silica	[45]
7	273	–	23.30	ion-imprinted polymer-based adsorbents	[46]
2	298	150	22.33	Ion imprinted mesoporous silica materials	[47]
5	320	60	51.5	Diethylenetriamine-functionalized chitosan magnetic nanobased particles	[48]
5	300	240	8.9–17.6	Magnetic-chitosan nano-based particles grafted with amino acids	[49]
6	–	–	22.00	Oxidized multi-walled carbon nanotubes	[50]
3.5	298	180	0.16	Vermiculite	[51]
5	298	90	37.04	11-molybdo-vanadophosphoric acid supported on Zr modified silica SBA-15	[52]
7	298	420	430.4	Hierarchical porous zeolitic imidazolate frameworks	[53]
6	298	90	35	LTA Zeolite	This work

zeolite exhibits comparable adsorption properties for adsorption of Dy^{3+} at room temperature, and lower contact time.

3.5. Adsorption mechanisms

Fig. 9 exhibit the dysprosium adsorbed quantity as a function of the square root of time t for the different temperatures studied. The multi-linearity found is commonly attributed to the presence of two or more mass transfer mechanisms that control the adsorption process [54].

In the present study, the dysprosium adsorption process onto the functionalized-zeolite shows three stages which could be attributed to each linear part [16]. First stage can be assigned to the diffusion of the adsorbed specie through the film which covering the adsorbent particles, and the adsorption of the adsorbate at the external surface of the adsorbent. The second stage can be attributed to the intraparticle diffusion. The second linear segment is the kinetic rate-determining step of the adsorption process because of this stage is a slow step (see Table 6). The third step can be assigned to the diffusion of the dysprosium through the adsorbent, followed by the establishment of equilibrium.

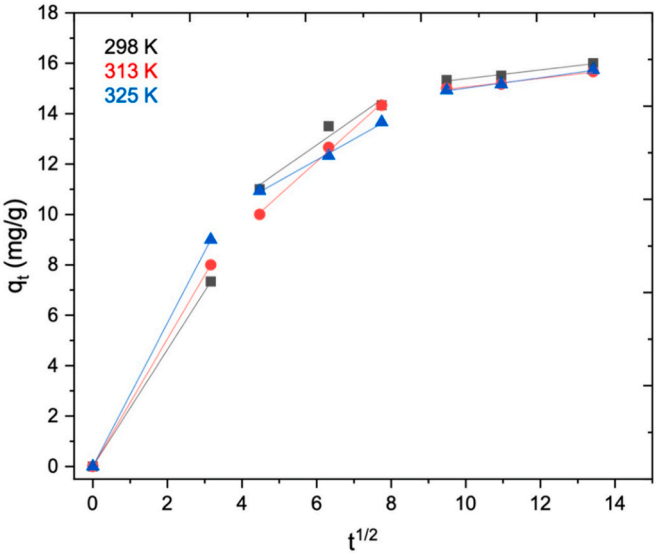

Fig. 9. Weber–Morris intraparticle kinetic adsorption curve for the different temperatures.

Table 6
Calculated rate constants from Weber–Morris intraparticle diffusion model.

Temperature (K)	k (mg·g^{-1}·min^{-1})[a]
298	1.03
313	1.33
325	0.85

[a] Second stage.

3.6. Raman measurements and magnetic recovery of the zeolites after Dy adsorption

Raman measurements were performed on the zeolite samples after the Dy adsorption, in order to confirm the stability at the selected pH of 6. For most of the recorded spectra, no evident differences are observed respect to the spectrum presented in Fig. 4. However, in some cases an extra band located at 458 cm^{-1} appears (Fig. 10). This band can be associated with a distortion of the aluminosilicate framework due to de adsorption of the Dy ions. This observation is in accordance with Dutta et al. [55], who observed an increase in the intensity of a broad band at 450 cm^{-1} for an amorphous aluminosilicate solid phase. On the other hand, VSM measurements of the Dy loaded zeolite are similar to the original material.

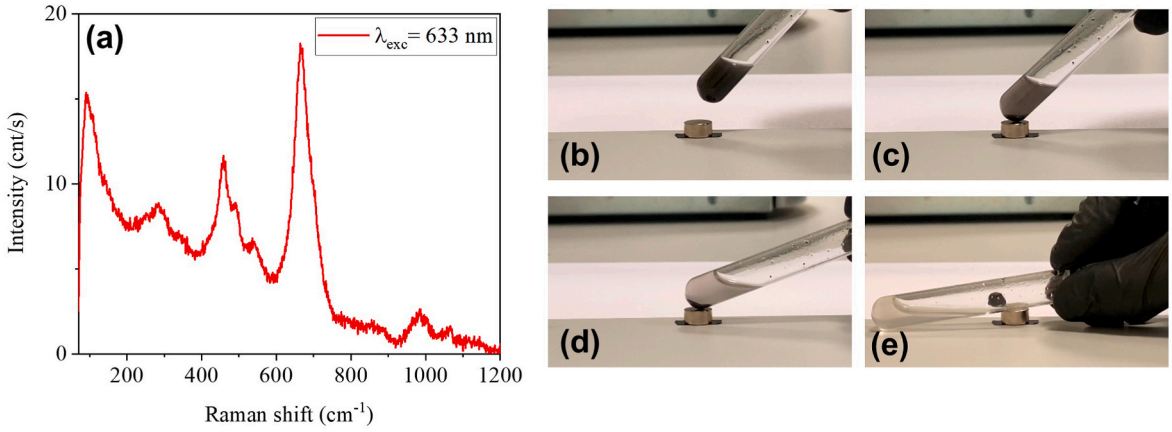

Fig. 10. (a) Raman spectrum recorded on the zeolite with Dy ions adsorbed. (b)–(e) Different steps of the recovery from the solution of the zeolite with a magnet. A video of the complete process can be seen in the supplementary material.

Finally, a neodymium magnet has been used to check the possibility to recover the zeolite with Dy sample from a solution. Images of the recovery of the sample can be found in Fig. 10b–e. In a few seconds, the sample is separated from the distilled water, and the adsorbed ions separated from the solution. A video of the process can be found in the Supplementary Material.

4. Conclusions

LTA Zeolite was synthesized using a hydrothermal method and functionalized with nanomagnetite. The zeolite was fully characterized to determine the morphology, crystal structure and efficient functionalization. The zeolite was employed to recover dysprosium from liquid solutions through an adsorption process. Initial tests at acidic pH, where Dy^{3+} predominates, showed low adsorption percentages (less than 5%). However, the dysprosium adsorption significantly increased when the tests were conducted at a higher pH value of 6, reaching almost 100% adsorption. The maximum adsorption capacity of the zeolite for Dy was approximately 35 mg g^{-1}.

Tests at different temperatures revealed that temperature had minimal effect on the adsorption capacity of the zeolite. The best fit for the experimental data was observed with the pseudo-second order kinetic model, with increasing kinetic constants at higher temperatures. Both Langmuir and Temkin isotherm models give good fitting of the experimental results, being slightly better the Temkin model. The thermodynamic parameters indicated that the dysprosium adsorption onto the zeolite was a spontaneous, and favorable process.

These results demonstrate that Dy can be efficiently recovered from aqueous solutions using our synthetic zeolite. Moreover, the functionalization of the zeolite with nanomagnetite allows for easy separation of the sample from the solution using a magnet.

CRediT authorship contribution statement

Lorena Alcaraz: Writing – review & editing, Writing – original draft, Visualization, Validation, Methodology, Investigation, Formal analysis, Data curation. **Belen Sotillo:** Writing – review & editing, Writing – original draft, Visualization, Supervision, Project administration, Methodology, Investigation, Funding acquisition. **Carlos Iglesias:** Writing – review & editing, Writing – original draft, Visualization, Validation, Investigation, Formal analysis. **Félix A. López:** Writing – review & editing, Resources, Project administration, Funding acquisition. **Paloma Fernández:** Writing – review & editing, Visualization, Supervision, Resources, Project administration. **Claudia Belviso:** Writing – review & editing, Visualization, Resources, Methodology, Investigation, Conceptualization. **Ana Urbieta:** Writing – review & editing, Validation, Supervision, Project administration, Methodology, Investigation, Conceptualization.

Declaration of competing interest

The authors declare that they have no known competing financial interests or personal relationships that could have appeared to influence the work reported in this paper.

Data availability

Data will be made available on request.

Acknowledgements

The authors are grateful to the Comunidad de Madrid for support via the Project PR65/19–22464 (Proyectos de I + D para jóvenes doctores). B. Sotillo acknowledges financial support from Comunidad de Madrid (Ayudas del Programa de Atracción de Talento 2017-T2/IND-5465). This work has been partially financed by the RC Metals Project 202260E098-CSIC.

Appendix A. Supplementary data

Supplementary data to this article can be found online at https://doi.org/10.1016/j.micromeso.2023.112843.

References

[1] L. Alcaraz, D.N. Saquinga, F.J. Alguacil, E. Escudero, F.A. López, Application of activated carbon obtained from spent coffee ground wastes to effective terbium recovery from liquid solutions, Metals (Basel) 11 (2021) 630, https://doi.org/10.3390/met11040630.
[2] L. Alcaraz, M.E. Escudero, F.J. Alguacil, I. Llorente, A. Urbieta, P. Fernández, F. A. López, Dysprosium removal from water using active carbons obtained from spent coffee ground, Nanomaterials 9 (2019) 1372, https://doi.org/10.3390/nano9101372.
[3] F. Alguacil, L. Alcaraz, I. García-Díaz, F. López, Removal of Pb2+ in wastewater via adsorption onto an activated carbon produced from winemaking waste, Metals (Basel) 8 (2018) 697, https://doi.org/10.3390/met8090697.
[4] Ó. Barros, L. Costa, F. Costa, A. Lago, V. Rocha, Z. Vipotnik, B. Silva, T. Tavares, Recovery of rare earth elements from wastewater towards a circular economy, Molecules 24 (2019) 1005, https://doi.org/10.3390/molecules24061005.
[5] S. Hoenderdaal, L. Tercero Espinoza, F. Marscheider-Weidemann, W. Graus, Can a dysprosium shortage threaten green energy technologies? Energy 49 (2013) 344–355, https://doi.org/10.1016/J.ENERGY.2012.10.043.
[6] A.K. Mosai, L. Chimuka, E.M. Cukrowska, I.A. Kotzé, H. Tutu, The recovery of rare earth elements (REEs) from aqueous solutions using natural zeolite and bentonite, water, Air. Soil Pollut. 230 (2019), https://doi.org/10.1007/s11270-019-4236-4.
[7] M. Moshoeshoe, M. Silas Nadiye-Tabbiruka, V. Obuseng, A review of the chemistry, structure, properties and applications of zeolites, Am. J. Mater. Sci. (2017) 196–221, https://doi.org/10.5923/j.materials.20170705.12, 2017.

[8] A. Khaleque, M.M. Alam, M. Hoque, S. Mondal, J. Bin Haider, B. Xu, M.A.H. Johir, A.K. Karmakar, J.L. Zhou, M.B. Ahmed, M.A. Moni, Zeolite synthesis from low-cost materials and environmental applications: a review, Environ. Adv. 2 (2020), 100019, https://doi.org/10.1016/J.ENVADV.2020.100019.

[9] C. Baerlocher, L.B. McCusker, Database of zeolite structures, n.d. http://www.iza-structure.org/databases/.

[10] F. Collins, A. Rozhkovskaya, J.G. Outram, G.J. Millar, A critical review of waste resources, synthesis, and applications for Zeolite LTA, Microporous Mesoporous Mater. 291 (2020), 109667, https://doi.org/10.1016/J.MICROMESO.2019.109667.

[11] C. Belviso, C. Cannas, N. Pinna, F. Cavalcante, A. Lettino, P. Lotti, G.D. Gatta, Effect of red mud added to zeolite LTA synthesis: where is Fe in the newly-formed material? Microporous Mesoporous Mater. 298 (2020), 110058 https://doi.org/10.1016/J.MICROMESO.2020.110058.

[12] European comission green deal, n.d. https://commission.europa.eu/strategy-and-policy/priorities-2019-2024/european-green-deal_en.

[13] G. Pascual-Muñoz, R. Calero-Berrocal, M. Larriba, V.I. Águeda, J.A. Delgado, Influence of sodium and potassium proportion on the adsorption of methanol and water on LTA zeolites at high temperature, Microporous Mesoporous Mater. 360 (2023), 112669, https://doi.org/10.1016/J.MICROMESO.2023.112669.

[14] S. Lagergren, Zur theorie der Sogenannten adsorption gelöster stoffe, kungliga svenska vetenskapsakademiens, Handlingar 24 (1898) 1–39.

[15] Y. Ho, G. McKay, Pseudo-second order model for sorption processes, Process Biochem. 34 (1999) 451–465, https://doi.org/10.1016/S0032-9592(98)00112-5.

[16] É.C. Lima, M.H. Dehghani, A. Guleria, F. Sher, R.R. Karri, G.L. Dotto, H.N. Tran, Adsorption: fundamental aspects and applications of adsorption for effluent treatment, in: Green Technol. Defluoridation Water, Elsevier, 2021, pp. 41–88, https://doi.org/10.1016/B978-0-323-85768-0.00004-X.

[17] G.S. Dos Reis, B. Grigore Cazacliu, C. Rodriguez Correa, E. Ovsyannikova, A. Kruse, C. Hoffmann Sampaio, E.C. Lima, G.L. Dotto, Adsorption and recovery of phosphate from aqueous solution by the construction and demolition wastes sludge and its potential use as phosphate-based fertiliser, J. Environ. Chem. Eng. 8 (2020), 103605, https://doi.org/10.1016/J.JECE.2019.103605.

[18] A.M. Aljeboree, A.N. Alshirifi, A.F. Alkaim, Kinetics and equilibrium study for the adsorption of textile dyes on coconut shell activated carbon, Arab. J. Chem. 10 (2017) S3381–S3393, https://doi.org/10.1016/j.arabjc.2014.01.020.

[19] K.H. Chu, Revisiting the Temkin isotherm: dimensional inconsistency and approximate forms, Ind. Eng. Chem. Res. 60 (2021) 13140–13147, https://doi.org/10.1021/acs.iecr.1c01788.

[20] S.M. Kamyab, C.D. Williams, Pure zeolite LTJ synthesis from kaolinite under hydrothermal conditions and its ammonium removal efficiency, Microporous Mesoporous Mater. 318 (2021), 111006, https://doi.org/10.1016/J.MICROMESO.2021.111006.

[21] X. Pang, L. Sellaoui, D. Franco, M.S. Netto, J. Georgin, G. Luiz Dotto, M.K. Abu Shayeb, H. Belmabrouk, A. Bonilla-Petriciolet, Z. Li, Preparation and characterization of a novel mountain soursop seeds powder adsorbent and its application for the removal of crystal violet and methylene blue from aqueous solutions, Chem. Eng. J. 391 (2020), 123617, https://doi.org/10.1016/J.CEJ.2019.123617.

[22] Y. Liu, Is the free energy change of adsorption correctly calculated? J. Chem. Eng. Data 54 (2009) 1981–1985, https://doi.org/10.1021/je800661q.

[23] E.C. Lima, A. Hosseini-Bandegharaei, J.C. Moreno-Piraján, I. Anastopoulos, A critical review of the estimation of the thermodynamic parameters on adsorption equilibria. Wrong use of equilibrium constant in the Van't Hoof equation for calculation of thermodynamic parameters of adsorption, J. Mol. Liq. 273 (2019) 425–434, https://doi.org/10.1016/J.MOLLIQ.2018.10.048.

[24] W.W. J, M.J. Carrell, Kinetics of adsorption on carbon from solution, J. Sanit. Eng. Div. 89 (1963) 31–59, https://doi.org/10.1061/JSEDAI.0000430.

[25] P.P. Knops-Gerrits, D.E. De Vos, E.J.P. Feijen, P.A. Jacobs, Raman spectroscopy on zeolites, Microporous Mater. 8 (1997) 3–17, https://doi.org/10.1016/S0927-6513(96)00088-0.

[26] Y. Yu, G. Xiong, C. Li, F.S. Xiao, Characterization of aluminosilicate zeolites by UV Raman spectroscopy, Microporous Mesoporous Mater. 46 (2001) 23–34, https://doi.org/10.1016/S1387-1811(01)00271-2.

[27] F. Fengtao, F. Zhaochi, L. Can, UV Raman spectroscopic study on the synthesis mechanism and assembly of molecular sieves, Chem. Soc. Rev. 39 (2010) 4794–4801, https://doi.org/10.1039/c0cs00012d.

[28] D.L.A.A. De Faria, S. Venâncio Silva, M.T. De Oliveira, Raman microspectroscopy of some iron oxides and oxyhydroxides, J. Raman Spectrosc. 28 (1997) 873–878, https://doi.org/10.1002/(sici)1097-4555(199711)28:11<873::aid-jrs177>3.0.co;2-b.

[29] Y.S. Li, J.S. Church, A.L. Woodhead, Infrared and Raman spectroscopic studies on iron oxide magnetic nano-particles and their surface modifications, J. Magn. Magn Mater. 324 (2012) 1543–1550, https://doi.org/10.1016/J.JMMM.2011.11.065.

[30] C. Yuan, Q. Liu, H. Chen, A. Huang, Mussel-inspired polydopamine modification of supports for the facile synthesis of zeolite LTA molecular sieve membranes, RSC Adv. 4 (2014) 41982–41988, https://doi.org/10.1039/C4RA05400H.

[31] A. Jacas-Rodríguez, P. Rodríguez-Pascual, D. Franco-Manzano, L. Contreras, C. Polop, M.A. Rodriguez, Mixed matrix membranes prepared from polysulfone and Linde type A zeolite, Sci. Eng. Compos. Mater. 27 (2020) 236–244, https://doi.org/10.1515/secm-2020-0022.

[32] C. Blanco, F. González, C. Pesquera, I. Benito, S. Mendioroz, J.A. Pajares, Differences between one aluminic palygorskite and another magnesic by infrared spectroscopy, Spectrosc. Lett. 22 (1989) 659–673, https://doi.org/10.1080/00387018908053926.

[33] S. Imashuku, K. Ono, R. Shishido, S. Suzuki, K. Wagatsuma, Cathodoluminescence analysis for rapid identification of alumina and MgAl2O4 spinel inclusions in steels, Mater, Character 131 (2017) 210–216, https://doi.org/10.1016/J.MATCHAR.2017.07.016.

[34] M. Ray, S. Sarkar, N.R. Bandyopadhyay, S.M. Hossain, A.K. Pramanick, Silicon and silicon oxide core-shell nanoparticles: structural and photoluminescence characteristics, J. Appl. Phys. 105 (2009), 74301, https://doi.org/10.1063/1.3100045.

[35] M. Zhu, Y. Han, R.B. Wehrspohn, C. Godet, R. Etemadi, D. Ballutaud, The origin of visible photoluminescence from silicon oxide thin films prepared by dual-plasma chemical vapor deposition, J. Appl. Phys. 83 (1998) 5386–5393, https://doi.org/10.1063/1.367407.

[36] D.W. Breck, Zeolite Molecular Sieves: Structure, Chemistry, Wiley, 1973.

[37] R. Qadeer, J. Hanif, Adsorption of dysprosium ions on activated charcoal from aqueous solutions, Carbon N. Y. 33 (1995) 215–220, https://doi.org/10.1016/0008-6223(94)00135-M.

[38] S. Feng, X. Du, M. Bat-amgalan, H. Zhang, N. Miyamoto, N. Kano, Adsorption of rees from aqueous solution by EDTA-Chitosan modified with zeolite imidazole framework (ZIF-8), Int. J. Mol. Sci. 22 (2021), https://doi.org/10.3390/ijms22073447.

[39] C. Belviso, M. Abdolrahimi, D. Peddis, E. Gagliano, M. Sgroi, A. Lettino, P. Roccaro, F.G.A. Vagliasindi, P.P. Falciglia, G. Di Bella, M.G. Giustra, F. Cavalcante, Synthesis of zeolite from volcanic ash: characterization and application for cesium removal, Microporous Mesoporous Mater. 319 (2021), 111045, https://doi.org/10.1016/J.MICROMESO.2021.111045.

[40] E.C. Lima, F. Sher, A. Guleria, M.R. Saeb, I. Anastopoulos, H.N. Tran, A. Hosseini-Bandegharaei, Is one performing the treatment data of adsorption kinetics correctly? J. Environ. Chem. Eng. 9 (2021), 104813 https://doi.org/10.1016/j.jece.2020.104813.

[41] J.S. Piccin, T.R.S. Cadaval, L.A.A. de Pinto, G.L. Dotto, in: A. Bonilla-Petriciolet, D. I. Mendoza-Castillo, H.E. Reynel-Ávila (Eds.), Adsorption Isotherms in Liquid Phase: Experimental, Modeling, and Interpretations BT - Adsorption Processes for Water Treatment and Purification, Springer International Publishing, Cham, 2017, pp. 19–51, https://doi.org/10.1007/978-3-319-58136-1_2.

[42] O. Ferrandon, H. Bouabane, M. Mazet, Contribution à l'étude de la validité de différents modèles, utilisés lors de l'adsorption de solutés sur charbon actif, Rev. Des Sci. l'eau. 8 (1995) 183–200, https://doi.org/10.7202/705218ar.

[43] S. Brunauer, K.S. Love, R.G. Keenan, Adsorption of nitrogen and the mechanism of ammonia decomposition over iron catalysts, J. Am. Chem. Soc. 64 (1942) 751–758, https://doi.org/10.1021/ja01256a005.

[44] A. Kara, E. Demirbel, Kinetic, isotherm and thermodynamic analysis on adsorption of Cr(VI) ions from aqueous solutions by synthesis and characterization of magnetic-poly(divinylbenzene-vinylimidazole) microbeads, water, Air. Soil Pollut. 223 (2012) 2387–2403, https://doi.org/10.1007/s11270-011-1032-1.

[45] T. Kegl, I. Ban, A. Lobnik, A. Košak, Synthesis and characterization of novel γ-Fe2O3-NH4OH@SiO2(APTMS) nanoparticles for dysprosium adsorption, J. Hazard Mater. 378 (2019), 120764, https://doi.org/10.1016/J.JHAZMAT.2019.120764.

[46] E. Liu, X. Xu, X. Zheng, F. Zhang, E. Liu, C. Li, An ion imprinted macroporous chitosan membrane for efficiently selective adsorption of dysprosium, Sep. Purif. Technol. 189 (2017) 288–295, https://doi.org/10.1016/J.SEPPUR.2017.06.079.

[47] X. Zheng, E. Liu, F. Zhang, Y. Yan, J. Pan, Efficient adsorption and separation of dysprosium from NdFeB magnets in an acidic system by ion imprinted mesoporous silica sealed in a dialysis bag, Green Chem. 18 (2016) 5031–5040, https://doi.org/10.1039/C6GC01426G.

[48] A.A. Galhoum, M.G. Mahfouz, S.T. Abdel-Rehem, N.A. Gomaa, A.A. Atia, T. Vincent, E. Guibal, Diethylenetriamine-functionalized chitosan magnetic nano-based particles for the sorption of rare earth metal ions [Nd(III), Dy(III) and Yb (III)], Cellulose 22 (2015) 2589–2605, https://doi.org/10.1007/s10570-015-0677-0.

[49] A.A. Galhoum, A.A. Atia, M.G. Mahfouz, S.T. Abdel-Rehem, N.A. Gomaa, T. Vincent, E. Guibal, Dy(III) recovery from dilute solutions using magnetic-chitosan nano-based particles grafted with amino acids, J. Mater. Sci. 50 (2015) 2832–2848, https://doi.org/10.1007/s10853-015-8845-z.

[50] S.M.A. Koochaki-Mohammadpour, M. Torab-Mostaedi, A. Talebizadeh-Rafsanjani, F. Naderi-Behdani, Adsorption isotherm, kinetic, thermodynamic, and desorption studies of lanthanum and dysprosium on oxidized multiwalled carbon nanotubes, J. Dispers. Sci. Technol. 35 (2014) 244–254, https://doi.org/10.1080/01932691.2013.785361.

[51] G. de V. Brião, M.G. da Silva, M.G.A. Vieira, Expanded vermiculite as an alternative adsorbent for the dysprosium recovery, J. Taiwan Inst. Chem. Eng. 127 (2021) 228–235, https://doi.org/10.1016/J.JTICE.2021.08.022.

[52] H. Aghayan, A.R. Mahjoub, A.R. Khanchi, Samarium and dysprosium removal using 11-molybdo-vanadophosphoric acid supported on Zr modified mesoporous silica SBA-15, Chem. Eng. J. 225 (2013) 509–519, https://doi.org/10.1016/J.CEJ.2013.03.092.

[53] A.F. Abdel-Magied, H.N. Abdelhamid, R.M. Ashour, X. Zou, K. Forsberg, Hierarchical porous zeolitic imidazolate frameworks nanoparticles for efficient adsorption of rare-earth elements, Microporous Mesoporous Mater. 278 (2019) 175–184, https://doi.org/10.1016/J.MICROMESO.2018.11.022.

[54] M. Schwaab, E. Steffani, E. Barbosa-Coutinho, J.B. Severo Júnior, Critical analysis of adsorption/diffusion modelling as a function of time square root, Chem. Eng. Sci. 173 (2017) 179–186, https://doi.org/10.1016/j.ces.2017.07.037.

[55] P.K. Dutta, D.C. Shieh, Crystallization of zeolite A: a spectroscopic study, J. Phys. Chem. 90 (1986) 2331–2334.